Materials & Design 260 (2025) 114919

Contents lists available at ScienceDirect

Materials & Design

journal homepage: www.elsevier.com/locate/matdes

Exploration of interface microstructures in additively manufactured multimaterial based on Ni, and Cu alloys through a cost-effective strategy☆

Federico Larini *, Riccardo Casati, Silvia Marola, Maurizio Vedani

Department of Mechanical Engineering, Politecnico di Milano, Milan, Italy

ARTICLE INFO

Keywords:
Additive manufacturing
Laser Powder Bed Fusion
Multimaterial processing
Copper alloy
Inconel-625
Microstructure

ABSTRACT

This study investigates microstructural transitions between Inconel-625 and CuNiSiCr alloys, processed via multimaterial L-PBF on a carbon steel substrate. The objective is to understand interface properties and optimize process parameters to improve material transitions. Single-material printing trials revealed greater processing challenges with CuNiSiCr primarily due to copper's high reflectivity at the infrared laser wavelength, leading to lack-of-fusion defects. Conversely, Inconel-625 exhibited excellent processability, achieving a relative density of 99.37%. In multimaterial printing, applying intermediate Volumetric Energy Density parameters at the interface reduced defects and improved transition homogeneity. Microstructural analysis revealed a gradual variation in chemical composition, indicating significant elemental diffusion, along with grain-size heterogeneity, yet no evidence of interfacial cracking was observed. Although the primary focus of this work was the Inconel-625/CuNiSiCr interface, the adopted configuration also enabled a preliminary assessment of the interactions between the printed alloys and the steel substrate. These additional observations confirmed that distinct microstructural features arise depending on the deposited material, with CuNiSiCr showing a heterogeneous morphology and Inconel-625 forming a more continuous metallurgical bond. These findings highlight the potential of multimaterial L-PBF for advanced components, emphasizing the need for optimized transition region design to minimize defects and improve interface integrity.

1. Introduction

Multimaterial components, combining the properties of different materials within a single product, represent one of the most significant innovations related to additive manufacturing (AM) in the industrial sector. This approach leverages the unique characteristics of each material, optimizing performance such as mechanical strength, lightweight, corrosion resistance, and thermal or electrical conductivity. In an industrial context increasingly focused on sustainability and efficiency, multimaterial components play a key role in reducing costs and enhancing product performance in applications ranging from automotive to aerospace, electronics, and medical [1].

In recent years, AM has emerged as a groundbreaking and versatile method for producing multimaterial components, particularly metallic ones. Among the various AM techniques, Direct Energy Deposition (DED) and its subcategory, Laser Engineered Net Shaping (LENS), are established technologies that offer maturity and reliability. However, they have a lower dimensional accuracy compared to Laser Powder Bed Fusion (L-PBF), which benefits from a finer laser spot size and thinner layer thickness, enabling the fabrication of more complex structures [2–5]. Nonetheless, integrating different metal alloys using these technologies remains challenging due to the significant differences in physical and metallurgical properties, which can undermine the quality and durability of multimaterial interfaces [1]. One of the main obstacles arises from the incompatibility of phases formed when joining different metal alloys. Variations in crystal structure of different phases between adjacent materials can induce internal stresses upon cooling or thermal cycling, compromising the component's structural integrity. Additionally, the formation of brittle intermetallic compounds can weaken the interface, leaving the component susceptible to fracture under mechanical loads. To mitigate these problems, strategies such as compositional gradients to smooth the transition at interfaces, substrate preheating, and process parameters optimization have been proposed [1,5,6]. However, material selection remains a decisive factor, with compatibility between alloys being critical.

Steel-copper multimaterials are particularly appealing for industrial

☆ This article is part of a special issue entitled: 'Additive Manufacturing' published in Materials & Design.

* Corresponding author at: Department of Mechanical Engineering, Politecnico di Milano, 34 La Masa, Milan 20156, Italy.
E-mail address: federico.larini@polimi.it (F. Larini).

https://doi.org/10.1016/j.matdes.2025.114919
Received 21 February 2025; Received in revised form 24 September 2025; Accepted 10 October 2025
Available online 16 October 2025

applications due to their unique combination of mechanical strength with high thermal and electrical conductivity. These properties are essential for applications in heat exchangers, injectors and nozzles, and moulds subjected to heavy thermal and mechanical loads [7–9]. The processing of copper alloys via L-PBF, per se, presents distinct challenges. Copper's high thermal conductivity and infrared (IR) reflectivity, typical of laser sources of commercially available AM machines, hinder sufficient heat absorption, often leading to lack-of-fusion defects [10,11]. An additional difficulty for multimaterials arises from the limited mutual solubility of copper and steel. At room temperature, only a small fraction of copper (less than 2.5 % by weight) can dissolve into α-Fe [12]. This incompatibility results in the formation of distinct layers enriched in either Cu or Fe when the two metals are directly joined, thus producing a peculiar microstructure at the interface region and possibly impairing its integrity. Studies have identified copper as a contributor to solidification cracking in steel, attributed to a wide solidification range of the steel-copper system (with copper as the terminal liquid), and thermal property discrepancies between the two materials [13,14]. In small amounts, and for similar mechanisms, copper induces liquid metal embrittlement (LME), wherein immiscible liquid copper infiltrates the grain boundaries of the already solidified steel and promote cracking due to shrinkage stresses upon cooling of the solid steel ligaments. Furthermore, the significant mismatch in thermal expansion coefficients (CTE) of copper (approximately 17 μm/m·K) and steel (10–12 μm/m·K) generates substantial residual stresses at the interface [15]. These stresses often lead to formation of cracks, which typically propagate into the steel, further depleting the mechanical properties of the multimaterial component [7,9,16,17].

A promising approach to address these challenges is the introduction of an intermediate material to facilitate a smoother transition between two alloys. Zhang et al., for instance, proposed using Deloro 22, a Ni-based alloy as an interlayer in the production of multimaterial components through DED technology, specifically joining H13 tool steel and pure copper [18]. Nickel, with its intermediate thermal expansion coefficient (approximately 13 μm/m·K), effectively reduces thermal stresses at the interface, significantly mitigating the formation of cracks during cooling.

Nickel's effectiveness is further enhanced by its excellent compatibility with copper. Nickel and copper are fully miscible across all compositions, forming a stable, homogeneous solid solution devoid of brittle intermetallics [19]. Recent studies have further confirmed the robustness of such interfaces in Inconel 718–Cu multimaterials produced via LENS [20], as well as in IN718–CuCrZr joints fabricated by L-PBF, provided that process parameters are properly optimized [21]. Nevertheless, other works have reported that deposition sequence and mixing ratio strongly affect solidification morphology and crack susceptibility [22]. Similarly, the iron-nickel system exhibits strong compatibility, with the formation of a stable solid solution across extensive regions of the phase diagram and no critical intermetallic compounds that could compromise the interface [23]. However, the presence of alloying elements may compromise interface stability: while defect-free steel–Inconel interfaces have been documented [24], several studies report cracking phenomena associated with microstructural defects and the formation of brittle phases, such as carbides and Laves phases [25,26].

This study focuses on the production of multimaterial components using L-PBF technology, specifically coupling a copper alloy (CuNiSiCr.02) with a nickel-based alloy (Inconel-625). The CuNiSiCr.02 alloy was selected due to its wide diffusion and ease of processability by LPBF, while maintaining fairly good thermal properties. The deposition was carried out on a carbon steel substrate, which served as the build platform and, at the same time, allowed for the assessment of the bonding integrity between the deposited alloys and the underlying steel. Metallographic analyses are conducted to evaluate the resulting interfaces, with particular attention to the developed phases, using techniques such as Light Optical Microscopy (LOM), Scanning Electron Microscopy (SEM), and Energy Dispersive Spectroscopy (EDS). Additionally, X-ray Diffraction (XRD) analysis is performed to investigate the phase composition across the CuNiSiCr-Inconel-625 transition regions.

The printer used in this research was a standard L-PBF system configured with modified powder supply system that effectively enabled multimaterial sample production according to a simplified geometry. This innovative approach offers a practical and cost-efficient solution for preliminary studies on various alloy combinations, exploring different material pairings with minimal modification of equipment setup, broadening the accessibility and flexibility of L-PBF multimaterial investigations.

2. Materials and methods

The materials employed in this study include pre-alloyed nickel-based powder (Inconel-625) and copper-based powder (CuNiSiCr), both supplied by m4p material Solution GmbH and commercially available as m4p™ Ni-625.03 (15–45 μm) and m4p™ CuNiSiCr.02 (20–53 μm), respectively. The particle size distribution, flowability, and apparent density of the powders were provided by the manufacturer in accordance with ISO 13322–2, ASTM B964, and ISO 3923–1:18–05 standards. The measured values are summarized in Table 1.

The chemical composition of each feedstock was analyzed using Energy Dispersive Spectroscopy (EDS) on multiple particles. The average values obtained are summarized in Table 2 and are consistent with the composition specified by the manufacturer. The steel composition of the printing platform, corresponding to an AISI 1018 carbon steel, was analyzed with a Bruker Q4 Tasman optical emission spectrometer (OES), and its chemical composition is also reported in Table 2.

Sample fabrication via L-PBF was carried out using a Renishaw AM 250 system equipped with a Reduced Build Volume (RBV) unit. The samples were built directly on a non-preheated AISI 1018 steel build platform without support structures. To minimize oxygen contamination, the build chamber was flooded with argon gas during the process. A preliminary set of samples, each measuring $8 \times 8 \times 10\ mm^3$, was printed using single powders to optimize process parameters for each material. The resulting density was measured via the Archimedean method using a Mettler Toledo ME analytical balance. After optimization, the following parameters were applied for both alloys: laser power of 200 W, layer thickness of 40 μm, hatch distance of 90 μm, and a bi-directional scanning strategy with a 67° rotation of the scan vector between layers [27]. In the Renishaw AM 250, which uses a pulsed rather than a continuous laser source, the scan path is controlled by two key parameters: the exposure time, corresponding to the duration of each laser pulse on a point, and the point distance, defined as the step between successive pulses along the scan track. The combination of these two parameters determines the effective scanning speed and the energy input delivered to the powder bed. Specifically, exposure time and point distance were set to 100 μs and 80 μm for Inconel-625, and 160 μs and 40 μm for CuNiSiCr, respectively. These settings correspond to Volumetric Energy Densities (VED) of 69 J/mm^3 for Inconel-625 and 222 J/mm^3 for CuNiSiCr [28].

To enable multimaterial printing, a custom-designed thin sheet (thickness 0.2 mm) acting as a divider of the powder feedstock platform was inserted within the dosing tank, positioned perpendicularly to the recoater and temporarily held in place with tape (Fig. 1). This divider physically separated the volume of the tank into two compartments, allowing one side to be filled with CuNiSiCr powder and the other with Inconel-625 powder.

Table 1
Physical properties of the feedstock material investigated.

Powder	d10 [μm]	d50 [μm]	d90 [μm]	Flow (∅ 5 mm) [s/50 g]	App. D. (∅ 5 mm) [g/cm^3]
Inconel-625	25	34	43	3	4.28
CuNiSiCr	19	34	55	15	4.92

Table 2
Chemical composition (in weight %) of Inconel-625 and CuNiSiCr feedstocks determined by EDS and steel printing platform analyzed by OES.

Powder	Ni	Cr	Mo	Nb	Mn	C	Fe	Si	Cu
Inconel-625	Bal.	22.25	8.90	3.52	–	–	2.62	–	–
CuNiSiCr	2.90	0.46	–	–	–	–	–	0.76	Bal.
AISI 1018	–	0.13	–	–	0.81	0.17	Bal.	0.27	0.06

After filling, the tape and partition plate were carefully removed to preserve the integrity of the powder boundary. The setup ensured that the powder transition zone was centered in the dosing tank and aligned with the center of the build platform. Four multimaterial samples, each measuring $8 \times 21 \times 10$ mm^3, were fabricated, as shown in Fig. 2a. Each sample was designed as a combination of three partially overlapping reference volumes using distinct parameters: two $8 \times 8 \times 10$ mm^3 blocks located entirely in the CuNiSiCr and Inconel-625 single-alloy volumes, and a transition block measuring $8 \times 9 \times 10$ mm^3. The transitional block overlapped the other two blocks by 2 mm to improve the structural continuity after printing (Fig. 2b).

During multimaterial printing, each block composed of a single material was fabricated using the optimized parameters previously identified. In contrast, the parameters for the interface region were varied to identify optimal printing conditions. Specifically, while laser power (200 W), layer thickness (40 μm), and hatch distance (0.090 mm) were held constant, exposure time and point distance were adjusted between 130–160 μs and 40–50 μm, respectively, corresponding to VED values of 144 J/mm^3, 194 J/mm^3, 208 J/mm^3, and 222 J/mm^3. A second set of multimaterial samples was fabricated by reducing the layer thickness to 30 μm while keeping the remaining parameters and the experimental layout unchanged, resulting in VED values of 193 J/mm^3, 259 J/mm^3, 278 J/mm^3, and 296 J/mm^3. The size of samples produced and analyzed was considered appropriate for the objective of this work, as it ensured a representative assessment of the Inconel-625/CuNiSiCr interface under the controlled experimental conditions investigated.

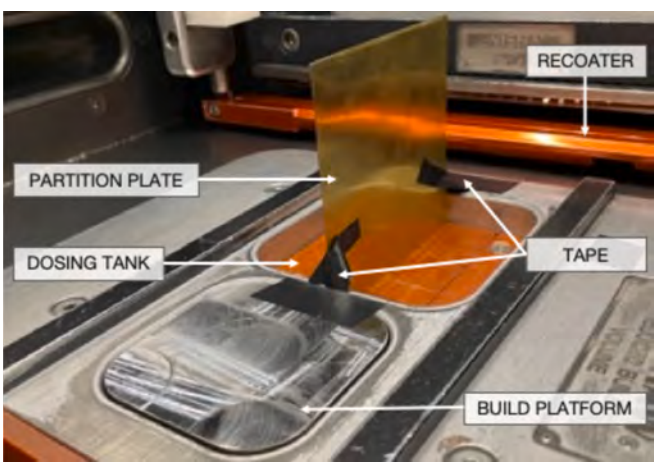

Fig. 1. Multimaterial setup for inserting two different powder feedstocks into the RBV dosing tank.

A precision abrasive wheel cutting saw was employed to produce sections of the printed platform, isolating each sample while maintaining the interface between the printed materials and the underlying steel substrate (Fig. 2b). Vickers microhardness tests were performed on the printed alloys using a load of 100 g and a dwell time of 15 s. For each single-material printing condition, the reported hardness value corresponds to the average of five measurements, carried out on single-material samples polished up to 1 μm. For the multimaterial configuration, individual hardness indentations were taken along the Inconel-625/CuNiSiCr interface, at 1 mm intervals and parallel to the build surface, on a polished cross-section prepared up to 1 μm. The metallographic preparation of the samples sectioned along the build direction involved grinding and polishing with a 50 nm colloidal silica suspension using an automated system. Microstructural analyses were subsequently performed using a Nikon Eclipse LV150NL optical microscope (LOM) and a Zeiss Sigma 500 field emission scanning electron microscope (FE-SEM) equipped with an Oxford Instruments Ultim Max energy dispersive spectroscopy (EDS) detector and an electron backscatter diffraction (EBSD) module.

X-ray diffraction (XRD) analyses were performed using a Rigaku SmartLab SE multipurpose diffractometer equipped with a D/teX Ultra 250 detector. The instrument utilized a copper radiation source with wavelengths of $k\alpha 1 = 1.541$ Å and $k\alpha 2 = 1.544$ Å, operating at a tube voltage of 40 kV and a tube current of 40 mA. Measurements were conducted on vertical cross-sections of multimaterial sample 4, fabricated with a layer thickness of 30 μm, focusing on three specific regions: the fully CuNiSiCr-composed zone, the fully Inconel-625 zone, and the interface between the two alloys. Diffraction patterns were collected with a step size of 0.02° and a scan speed of 0.2°/min for the interface region, while a scan speed of 1.3°/min was used for the homogeneous CuNiSiCr and Inconel-625 regions.

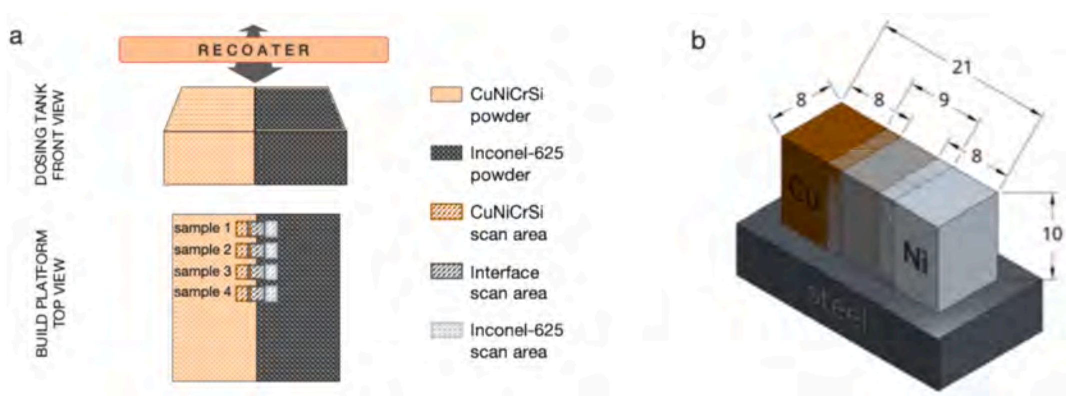

Fig. 2. Schematic of the manufacturing process for multi-material samples illustrating the arrangement of the samples on the build platform (a) and their final dimensions in mm (b). The labels "steel," "Cu," and "Ni" correspond to the materials used for the carbon steel build platform, the CuNiSiCr, and Inconel-625 alloys, respectively.

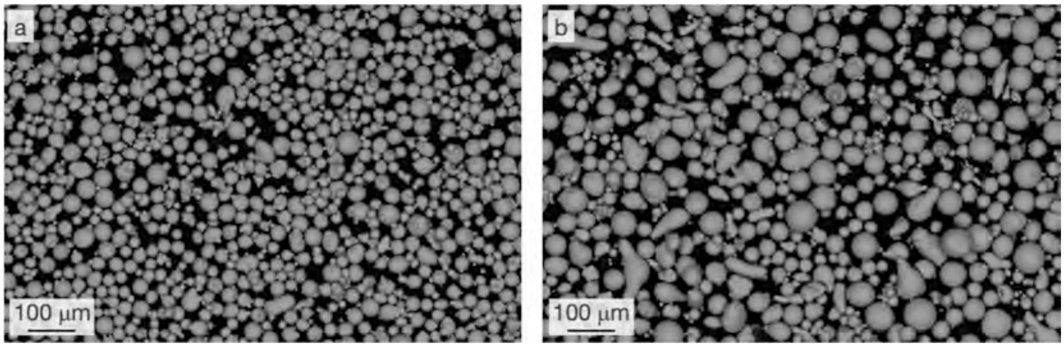

Fig. 3. SEM images of the Inconel-625(a) and CuNiSiCr (b) powder.

3. Results and discussion

3.1. Powder feedstock

Fig. 3 illustrates representative SEM images of the feedstock materials. Both powders exhibit smooth surfaces and high sphericity, particularly the Inconel-625 alloy. The particle size differences align with the supplier's specifications, with CuNiSiCr particles being, on average, larger than those of Inconel-625.

3.2. Single-material printing trials

Single-alloy samples were printed to identify the reference processing parameter sets for Inconel-625 and CuNiSiCr alloy. While Inconel-625 samples were successfully printed without technical issues, the CuNiSiCr printing process encountered interruptions approximately at mid-thickness of the printing stage due to optics overheating, attributed to the inability of the machine's cooling system to manage the high temperatures generated during copper processing. Copper's high reflectivity at the laser wavelength (1.07 μm) used by the Renishaw AM-250 L-PBF system, with an absorptivity of approximately 3 % [29], significantly limits the energy available for material melting, as over 95 % of the laser energy is reflected, leading to excessive heating of the optical path. Despite these difficulties, the densest copper-based samples reached a relative density of 96.39 % with a corresponding microhardness of 89 ± 6 $HV_{0.1}$, while Inconel-625 samples exhibited a maximum density of 99.37 % and a microhardness of 274 ± 6 $HV_{0.1}$. Figs. 4 and 6 present SEM images of the best samples produced.

Optimized parameters yielded fully dense Inconel-625 parts with sparse gas porosity measuring only a few microns (Fig. 4a). At higher magnification, a typical sub-cellular structure is observed, consisting of cells ranging from ~ 0.4 to 1.0 μm (Fig. 4b) in size. EDS maps reveal pronounced segregation of Nb and Mo along cell boundaries, forming a continuous interdendritic network (Fig. 4c–f). This phenomenon is well described in the literature for LPBF-processed Inconel-625 and is generally associated with the nucleation of Laves-type phases. The formation of carbides or oxides along the cellular walls has also been reported under specific conditions or following post-processing heat treatments [30].

EBSD analyses (Fig. 5) further confirm, for both investigated alloys (Inconel-625 and CuNiSiCr), the presence of large columnar grains predominantly aligned with the build direction.

In contrast, CuNiSiCr samples showed extensive lack of fusion (LoF) defects, with porosities up to 200 μm (Fig. 6a). Unmelted or partially melted powder particles were frequently observed within the LoF porosities, further indicating insufficient VED during processing. At higher magnifications, no distinctive precipitates or secondary phases were detected (Fig. 6b), while the chemical composition appeared essentially homogeneous.

No cracks were observed in any processed sample. Previous studies demonstrate that higher laser powers or lasers with shorter wavelengths can significantly improve absorption and enable the production of fully dense copper-based alloys [11,16,31,32]. Specifically, CuNiSiCr alloys have been successfully processed by L-PBF to achieve relative densities

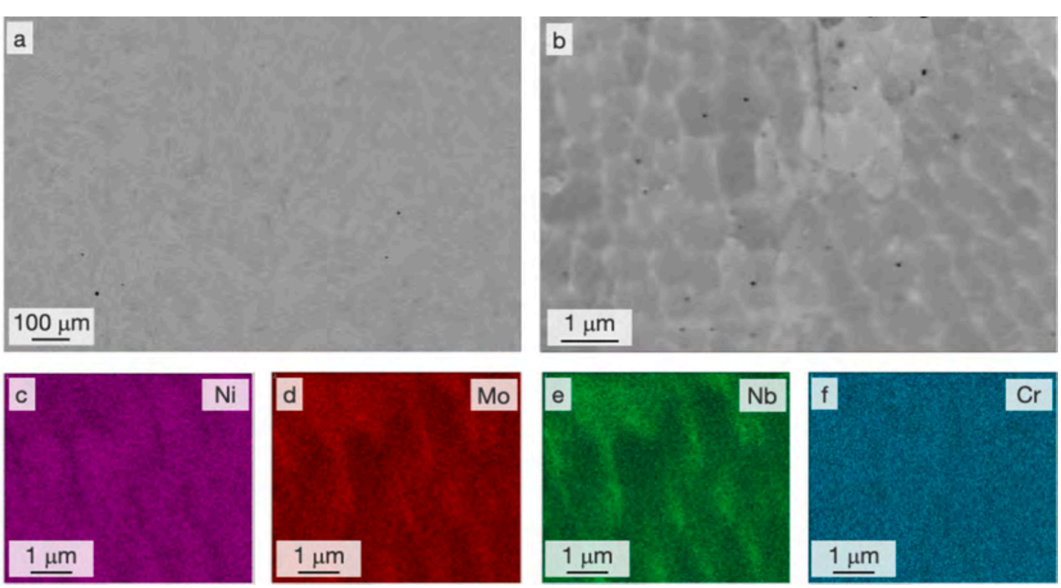

Fig. 4. Backscattered electron SEM images of Inconel-625 in the as-built condition at low (a) and high magnification (b), accompanied by EDS elemental maps (c–f).

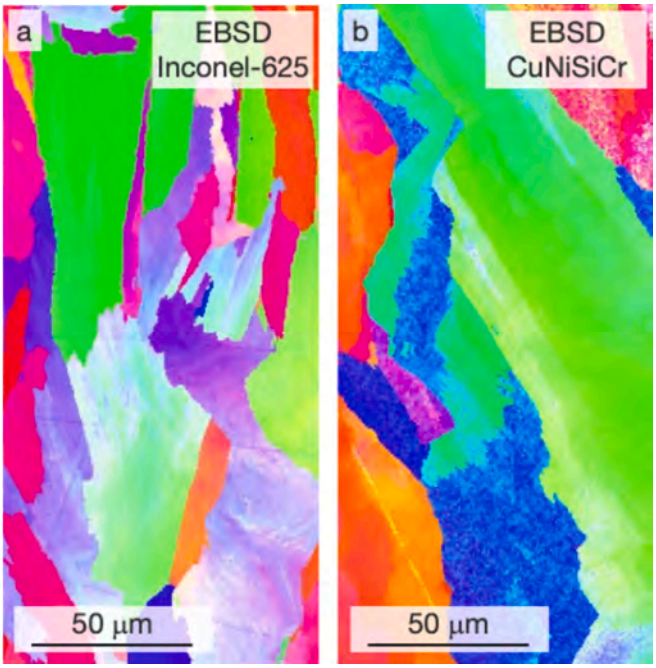

Fig. 5. EBSD orientation maps of Inconel-625 (a) and CuNiSiCr (b) in the as-built condition.

exceeding 99 % through appropriate parameter optimization [33]. Similarly, Inconel-625 is extensively reported as a highly processable alloy in LPBF, yielding high density and favorable mechanical properties when suitable parameters are employed [34]. Although multimaterial processing introduces additional challenges related to thermal gradients and residual stress fields, it remains feasible through a careful balance of scanning conditions [35,36]. Within this framework, the parameter set for CuNiSiCr.02 that provided the highest achievable relative density was deliberately adopted for the fabrication of the planned multimaterial samples, under the assumption that the presence of occasional LoF could not significantly impair the investigation, whose primary aim was to provide a preliminary assessment of interface integrity and quality in AM-processed multimaterial systems.

3.3. Multimaterial printing and optimization of transitions

Once defined the processing parameters of the 100 % CuNiSiCr and 100 % Inconel-625 volumes, the transition zones were printed with intermediate parameters to explore the impact of varying VED on microstructure. Table 3 summarizes the process parameters used for the two series of multimaterial printing, performed with layer thicknesses of 40 μm and 30 μm. To minimize variability and ensure a smooth transition, only the exposure time and point distance were adjusted, thereby generating different VED values in the interface regions. It should be noted that, in the same build, the parameters used for the fully Inconel-625 and fully CuNiSiCr zones were kept constant; the only variation among samples concerned the parameter set applied to the transition region. As summarized in the table, sample 1 maintained the fully CuNiSiCr VED values, while samples 2, 3, and 4 employed progressively reduced VED values (down to 35 %) to approach the fully Inconel-625 parameters.

Fig. 7 shows low-magnification LOM images of the multimaterial samples produced with the parameter sets reported in Table 3. It is confirmed that the processing of the CuNiSiCr alloy is more challenging and results in the presence of LoF porosity. Additionally, a distinct accumulation of porosity is noticed at the locations corresponding to interruptions of the 30 μm layer thickness printing process, as highlighted in the figure by the red arrows. Nevertheless, the higher VED levels applied in the 30 μm samples were effective in reducing overall porosity compared to the 40 μm samples.

In most of the parameter combinations, gas-induced porosities were identified in the interface region (highlighted by green arrows in Fig. 7). This phenomenon is linked to the use of VED values significantly higher than those optimized for the Inconel-625 single-material. Additionally, it can be supposed that the partial overlap between the interface region and the 100 % Inconel-625 zone resulted in a further overheating which would exacerbate the generation of porosity. Under such energy surplus

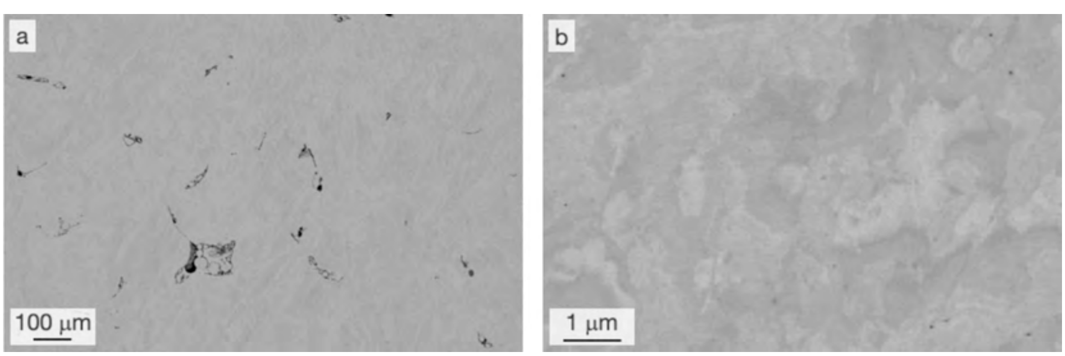

Fig. 6. Backscattered electron SEM images of CuNiSiCr in the as-built condition at low (a) and high magnification (b).

Table 3
Combinations of exposure time and point distance investigated for the Inconel-625 / CuNiSiCr multimaterial samples. Constant parameters are: laser power 200 W and hatch distance 90 μm.

Layer thickness [μm]	30			40		
	Exposure time [μs]	Point distance [μm]	VED [J/mm^3]	Exposure time [μs]	Point distance [μm]	VED [J/mm^3]
100 % Inconel-625	100	80	93	100	80	69
Interface sample 1	160	40	296	160	40	222
Interface sample 2	140	40	259	140	40	194
Interface sample 3	130	50	193	130	50	144
Interface sample 4	150	40	278	150	40	208
100 % CuNiSiCr	160	40	296	160	40	222

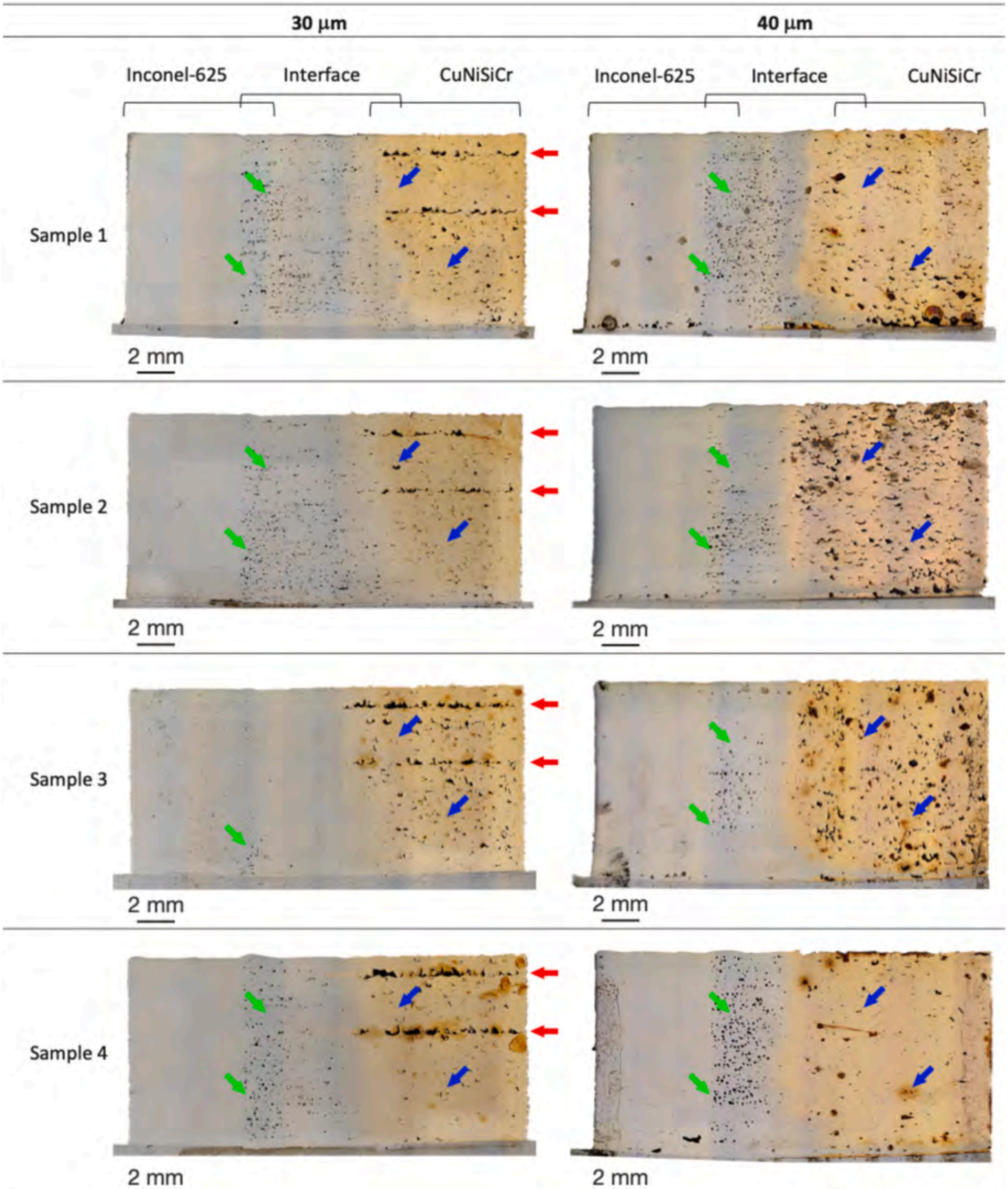

Fig. 7. LOM images of the investigated multimaterial samples: four fabricated with a layer thickness of 30 μm, and four with a layer thickness of 40 μm. At the top of the figure, the three partially overlapping regions used for the fabrication of all multimaterial samples are highlighted, corresponding to volumes produced with the printing parameters 100 % Inconel-625, 100 % CuNiSiCr, and Inconel-625/CuNiSiCr interface (see Table 3). Red arrows mark the two print interruptions experienced during the 30 μm layer thickness sample production; green arrows indicate typical gas-induced porosities; blue arrows highlight LoF defects. (For interpretation of the references to colour in this figure legend, the reader is referred to the web version of this article.)

conditions, phenomena reminiscent of keyhole mode solidification may occur, even at moderate laser powers, leading to unstable melt pool collapse and generate circular porosities containing trapped gas and vapors [37,38]. In sample 3, the reduced VED applied at the interface, with intermediate value between the VEDs of 100 % Inconel-625 and 100 % CuNiSiCr, demonstrated to provide the best compromise, minimizing gas porosity while maintaining a smoother transition between the two materials.

In summary, after a general assessment of sample integrity, sample 3 printed at 30 μm layer thickness demonstrated the most favorable properties and was selected for further investigation about interface characteristics.

3.4. Transition between Inconel-625 and CuNiSiCr alloy

Fig. 8b presents the average elemental concentrations measured by EDS approximately at mid-height of sample 3 (layer thickness: 30 μm), crossing the transition region separating the two alloys.

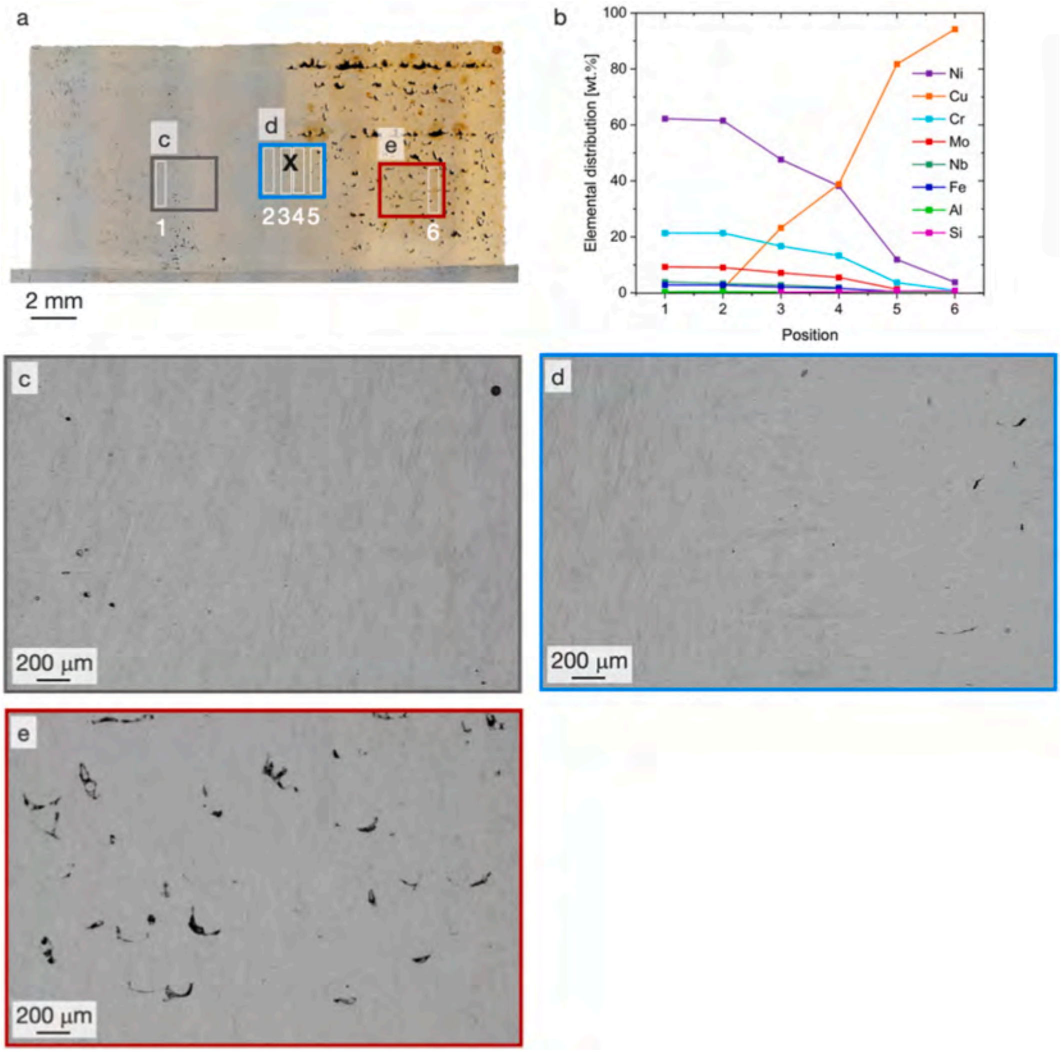

Fig. 8. LOM image of multimaterial sample 3 fabricated with 30 μm layer thickness (a). The average elemental distribution reported in the graph was obtain by analyzing rectangular areas of equal size located at positions 1–6 (b). The X position corresponds to the location of the combined EBSD and EDS elemental map analyses shown in Fig. 11. Magnified backscattered electron SEM views of the regions highlighted in the colored boxes display the microstructure of Inconel-625 (c), Inconel-625/CuNiSiCr transition zone (d) and CuNiSiCr alloy (e).

EDS analysis confirms that position 1 is entirely made of Inconel-625 alloy, with a chemical profile consistent with that of the base material (Table 2). Fig. 8c reveals the excellent processability of the Ni-base alloy, showing negligible amount of defects.

In the interface region, a gradual shift is observed from position 2, predominantly composed of Inconel-625 where the chemical concentrations remain stable except for the appearance of trace amounts of Cu, to position 5, almost entirely consisting of CuNiSiCr alloy. In this zone, the onset of the first LoF defects emerge. Throughout the transition, the concentrations of Ni, Cr, and Mo progressively decrease, as indicated by Fig. 8b, whereas the distribution of Cu progressively rises, reaching a complete transition to CuNiSiCr alloy over approximately 2.8 mm, suggesting significant elemental diffusion between the materials. Fig. 8d demonstrates a continuous metallurgical bond without cracks.

A series of Vickers microhardness measurements were performed along the Inconel-625/CuNiSiCr interface. As shown in Fig. 9, hardness values in the fully Inconel-625 region averaged around 290 $HV_{0.1}$, while those in the fully CuNiSiCr region stabilized at approximately 100 $HV_{0.1}$. Across the transition zone, the hardness decreased progressively from Inconel-625 toward CuNiSiCr, following the compositional gradient evidenced by the EDS analysis. These slightly higher hardness values, compared to those obtained for the single-alloy samples (274 $\pm$ 5.8 $HV_{0.1}$ for Inconel-625 and 89 $\pm$ 5.9 $HV_{0.1}$ for CuNiSiCr), could be partially influenced by the reduced layer thickness (30 μm instead of 40 μm). Overall, the measured profile confirms a gradual and continuous transition in mechanical response across the interface, consistent with the observed microstructural and chemical evolution.

XRD analysis (Fig. 10) confirm that both Cu-based and Ni-based regions at the interface crystallize in the primary fcc phase, as predicted by the Cu-Ni binary equilibrium phase diagram. The diffraction patterns

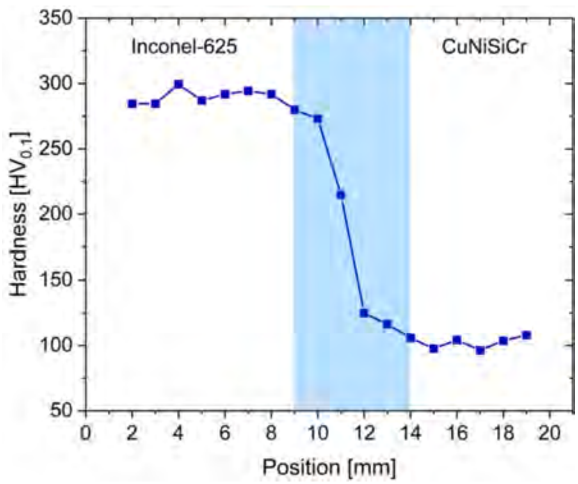

Fig. 9. Vickers microhardness profile across the Inconel-625/CuNiSiCr interface in multimaterial sample 3 (30 μm layer thickness). The shaded blue band highlights the progressive decrease in hardness values across the material transition. (For interpretation of the references to colour in this figure legend, the reader is referred to the web version of this article.)

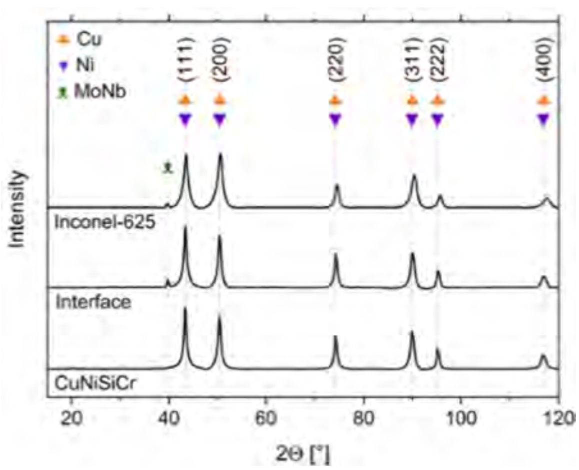

Fig. 10. XRD diffractograms of the multimaterial sample 4, produced with a layer thickness of 30 μm, acquired from the fully CuNiSiCr region, the fully Inconel-625 region, and the interface.

obtained from the fully CuNiSiCr region, the fully Inconel-625 region, and the transition region, all exhibit peaks corresponding to the primary fcc phase. However, a slight shift towards higher diffraction angles is observed in the Inconel-625 region compared to CuNiSiCr, likely due to differences in lattice parameters. In addition to the main fcc peaks, a weak reflection at ~ 40° was detected. This signal is consistent with the presence of Nb–Mo-rich secondary phases, as suggested by the segregation phenomena observed at cell boundaries in the high-magnification SEM and EDS analyses (Fig. 4). Such features are commonly reported in LPBF-processed Inconel-625 and are often associated with Laves-type compounds [39]. However, no further characteristic reflections were detected, which complicates a definitive phase assignment. Similar findings have been reported in previous studies, where rapid solidification and elemental segregation during LPBF promoted the nucleation of Laves phases, while their precise identification required higher-resolution techniques such as TEM [40].

Away from the interface, the microstructure of the CuNiSiCr alloy, visible in Fig. 8e, is characterized by frequent LoF defects, in agreement to results collected for the CuNiSiCr single-alloy samples. It is concluded that, despite the reduced layer thickness of 30 μm which was added to the investigated parameters in multimaterial printed samples, the energy input during scanning remains insufficient to achieve full melting.

Fig. 11 shows a collection of images taken at interface between Inconel-625 and CuNiSiCr alloys (position X in Fig. 8a) using EBSD and EDS detectors. Both crystal structure and elemental information suggest that the transition region between these two alloys becomes rather heterogeneous at the microscale. In contrast to the large columnar grains observed in the single-material samples (Fig. 5), the microstructure at the interface is markedly different. The grain structure reported in Fig. 11a highlights a bimodal grain size distribution, where coarse grains exceeding 100 μm coexist with extremely fine crystals smaller than 5 μm. These latter are mainly located on the Cu-rich side (right side in Fig. 11a) of the interface region. The distribution of elements displayed by the EDS maps (see Figs. 11b to 11e) gives evidence of distinct liquid melt streams of the two alloys at the stage of melt pool solidification, whereby Cu tends to occupy positions that are complementary to those of Ni, Cr and Mo. Therefore, while both alloys share the same fcc lattice, they should be regarded as chemically distinct regions within the interface, rather than a perfectly homogeneous single-phase solid solution.

To complete the microstructural characterization, a quantitative grain boundary analysis based on the misorientation distribution function (MDF) was performed in the transition region. The results show a strong dependence on local composition, reflecting the different metallurgical responses of the alloys during solidification and L-PBF thermal cycling. In Cu-enriched areas, high-angle grain boundaries (HAGB, >15°) dominate (~63 %), while low-angle boundaries (LAGB, 2–15°) account for ~ 27 %, with the remaining ~ 10 % corresponding to misorientations below 2°. This indicates a microstructure with well-defined grains and signs of localized recrystallization. In contrast, Ni–Cr–Mo–rich regions exhibit a nearly balanced distribution of LAGB (~49 %) and HAGB (~51 %), consistent with an intermediate microstructure combining sub-grains with high dislocation density and grains separated by high-angle boundaries.

3.5. Transition between steel substrate and CuNiSiCr alloy

A second type of transition is found between the AISI 1018 steel substrate and each of the two single alloys. The investigation was extended to these interface regions, considering that the mechanisms of formation of these mixed regions are different since, upon L-PBF processing, the alloys are deposited onto the substrate, inducing localized remelting of the solid steel, but only within a limited thickness and primarily in the first layers of deposited powder.

Fig. 12a shows a cross-section SEM image of the transition zone between the steel substrate and the upper part made of the CuNiSiCr alloy, taken along the build direction. On the top surface of the substrate, the melt pools generated by the laser tracks during the initial layer of the L-PBF process are clearly visible, highlighted by red arrows.

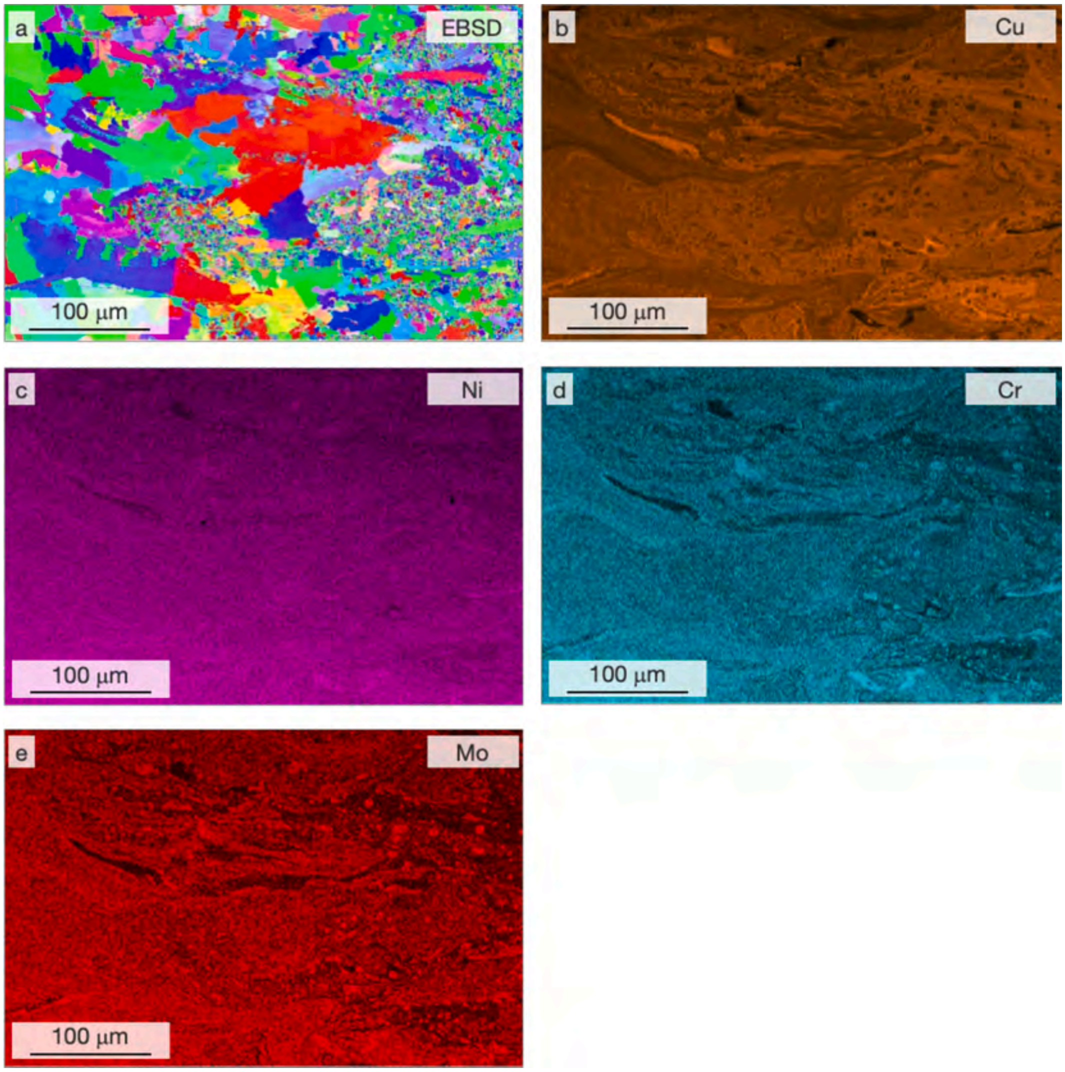

Fig. 11. Combined EBSD and EDS analyses of the interface region at the Inconel-625/CuNiSiCr transition zone. EBSD orientation map (a), EDS elemental maps (b-e).

It is to recall that Cu- and Fe-based alloys are almost insoluble already in the liquid stage [12]. Consequently, the immiscibility of the materials, combined with the rapid cooling characteristic of the L-PBF process leads to the formation of a unique microstructure. Distinct droplets of the steel-rich melt are separated from the low-melting Cu-rich alloy. The formers are supposed to solidify at an earlier stage, and become later surrounded by the copper-rich matrix. Fig. 12b clearly confirm this hypothesis, showing the globular microstructure formed by the darker steel globules embedded in the Cu-rich alloy. At higher magnifications, it becomes evident that the steel globules also contain smaller brighter particles of segregated Cu-alloy, as shown in Fig. 12c.

A second observed feature is represented by the segregation and/or infiltration of copper along the steel grain boundaries at the transition regions most close to the substrate. It is assumed that, when the amount of copper diluted with the steel melt decreases below a critical threshold, the microstructure shifts from the previously described globular morphology to a state where low-melting-point copper segregates at the grain boundaries (presumably when the steel is also subjected to resolidification) or partially infiltrates the exposed grains of the solid steel substrate. EDS point analyses (Table 4) confirm that the bright veins observed in the microstructure are copper-rich, supporting the hypothesis that these infiltrations originate from liquid copper solidifying at the boundaries of already solidified steel grains. During the last stages of solidification when shrinkage stresses build up across solid grains, the liquid copper films at boundaries become an easy path for crack growth, thus compromising the structural integrity at the interface. Evidence of this effects are depicted in Figs. 12b and 12d, highlighting the presence of bright veins at the steel grain boundaries and of cracks on a specific layer along the transition region [13,16,18,41].

Moving further away from the steel substrate, the cracks disappear, suggesting that the tendency to form hot-tears is closely related to a specific critical copper concentration range in the Fe-rich melt.

Fig. 13 further illustrates the elemental distribution maps at the steel-substrate interface, along with the pronounced dimensional

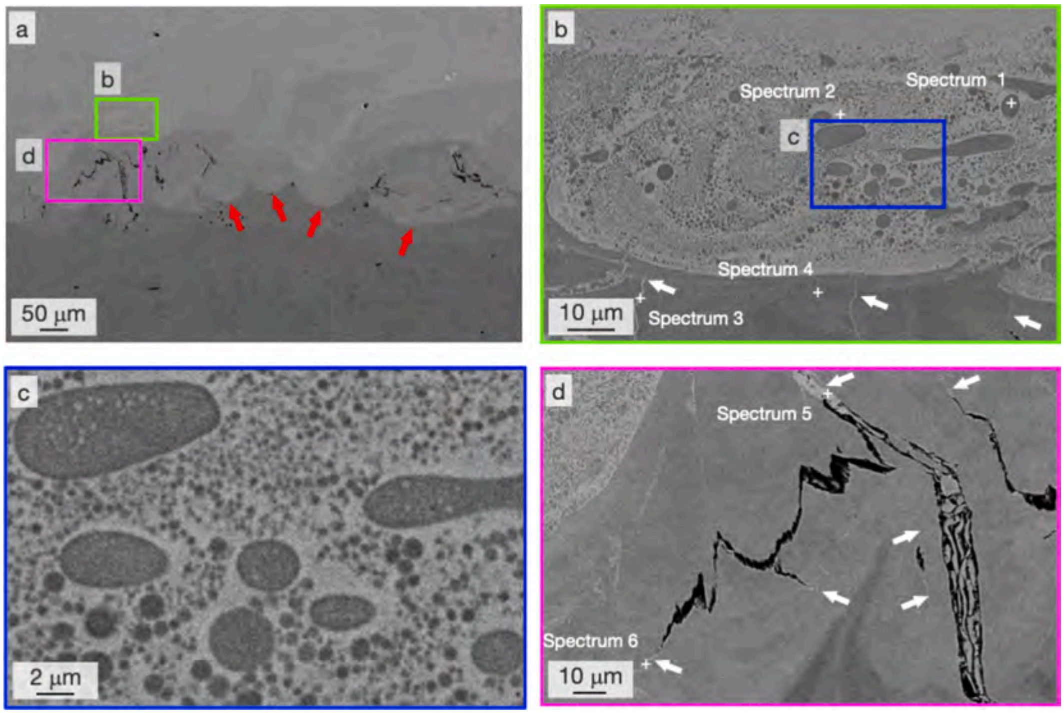

Fig. 12. Backscattered electron SEM images across the steel substrate/CuNiSiCr transition zone in Sample 3 (a). Red arrows indicate the profile of the former melt pools facing the solid steel substrate, while white arrows point to the copper-based veins. Magnified views of the areas in the colored boxes highlight microstructural features, including steel spheroidal particles embedded in the copper matrix (b) with fine copper precipitates within the coarser steel particles (c) and cracks at the interface (d). (For interpretation of the references to colour in this figure legend, the reader is referred to the web version of this article.)

Table 4
EDS measurements (in weight %) corresponding to the points indicated in Fig. 12.

Label	Fe	Cu	Ni	Cr	C	Other
Spectrum 1	71.20	24.62	2.39	0.72	–	–
Spectrum 2	6.90	91.82	0.95	–	–	–
Spectrum 3	24.72	73.37	1.13	–	–	0.38
Spectrum 4	55.64	42.19	0.96	0.23	–	0.54
Spectrum 5	8.10	75.58	0.72	–	15.60	–
Spectrum 6	38.02	51.35	1.82	0.60	8.21	–

difference between the two materials. The CuNiSiCr alloy exhibits fine grains with an average size of ~ 5 μm, whereas the steel is characterized by much coarser grains of approximately 30 μm. The chemical maps confirm the immiscibility of the two main elements. Iron is confined to the steel substrate with a bcc structure and in the dispersed spheroidal particles while the copper-rich region features an fcc crystal structure.

3.6. Transition between steel substrate and Inconel-625 alloy

A different situation is met when investigating the transition between the steel substrate and the Inconel-625 alloy. As already mentioned in the introduction, these two alloys show an extended mutual solubility also at the solid stage, at high temperatures [23].

Fig. 14 presents a typical SEM image of this transition zone. Also in this case, the melt pools generated by the laser tracks on the steel substrate during the initial layers of the L-PBF process are revealed (highlighted by red arrows in the figure).

Starting from that interface, the microstructure is subjected to a continuous shift from a Fe-rich alloy to the final Inconel-625 alloy without any sign of hot cracks.

Fig. 15 shows a collection of images taken at interface between steel substrate and Inconel-625 alloy using EBSD and EDS detectors. The chemical and phase maps suggest that an interdiffusion region with a thickness of about 30 μm is formed across the original interface, combining significant amount of Fe coming from the substrate with Ni, Cr, Mo and Nb brought by the Inconel-625 alloy.

This elemental distribution promotes the presence of an interlayer of fcc phase as a result of overalloying with Ni (a strong austenitizing element) of the steel structure which shifts from bcc to fcc in the transition zone [42].

The relatively thin interdiffusion zone indicates a rapid shift between the two alloys. In spite of this, the presence of an intermediate fcc steel layer facilitates a more gradual progression between the bcc steel substrate and the fcc structure of the Inconel-625 alloy, supposedly enhancing the strength and integrity of the bond. The grain structure at the transition region is depicted in the EBSD orientation map of Fig. 15a. In the fully Inconel-625 domain, columnar grains exceeding 100 μm in length are observed, displaying epitaxial growth and a preferential orientation along the build direction. Finally, extremely fine equiaxed grains, in some cases smaller than 5 μm, are observed in the upper part of the bcc steel substrate. These can be attributed to the melting of the substrate steel during the initial laser scans, combined with the high

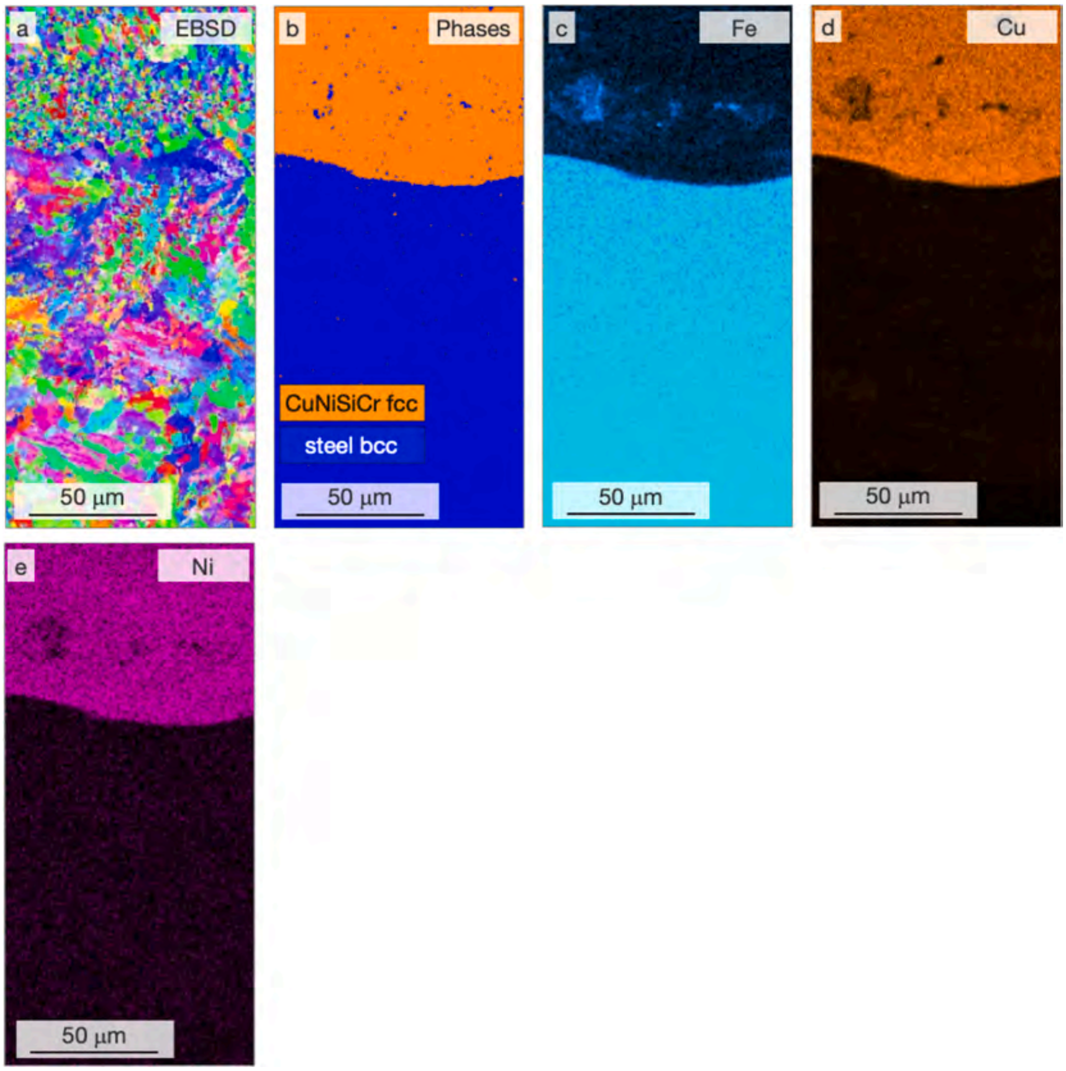

Fig. 13. Combined EBSD and EDS analyses collected at the steel substrate/CuNiSiCr transition zone. EBSD orientation map (a), phases map (b), EDS elemental maps (c-e).

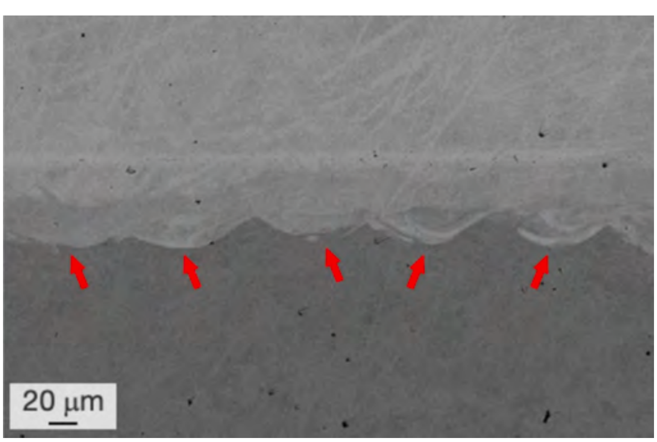

Fig. 14. Backscattered electron SEM image of the steel substrate/Inconel-625 transition zone in Sample 3. Red arrows indicate the former melt pools. (For interpretation of the references to colour in this figure legend, the reader is referred to the web version of this article.)

cooling rates typical of the L-PBF process [43].

4. Conclusions

This study investigated the quality of the microstructural transition regions between Inconel-625 and CuNiSiCr alloys, additively produced through multimaterial printing on a steel substrate. The key findings and conclusions are summarized as follows:

- An innovative simple, and cost-effective setup enabled the adoption of a commercial printer for the simultaneous printing of two materials, allowing the investigations of their transition regions. This approach is particularly valuable for preliminary metallurgical studies and can contribute to improve the understanding of the multimaterial-interface generation by L-PBF processing.
- The interface region of multimaterial printed parts requires specific process parameters that differ from those optimized for the individual materials. The application of an intermediate Volumetric Energy Density (VED) proved to be the most effective condition for minimizing flaws and ensuring a seamless transition between the two alloys.

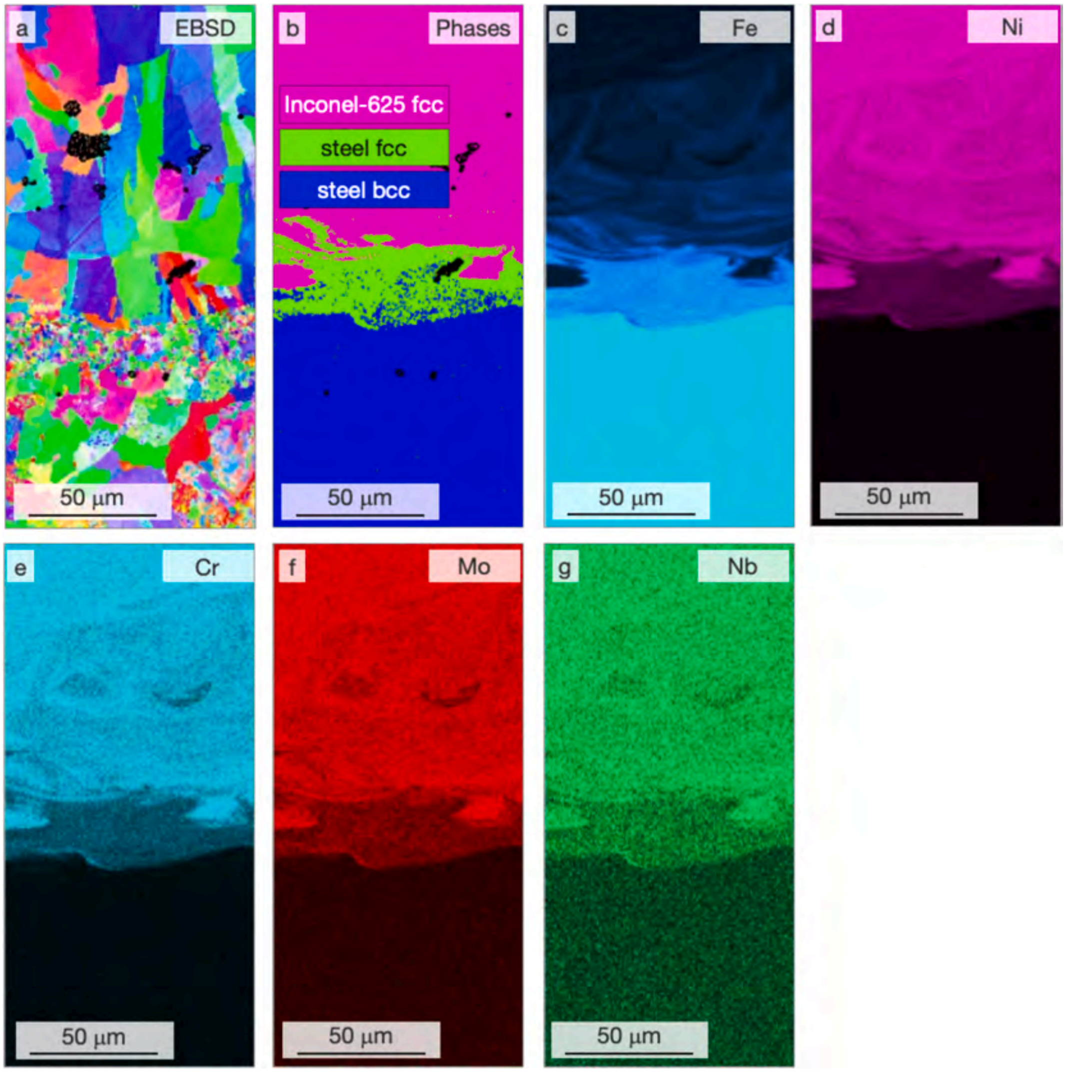

Fig. 15. Combined EBSD and EDS analyses collected at the steel substrate/Inconel-625 transition zone. EBSD orientation map (a), phases map (b), EDS elemental maps (c-g).

- Inconel-625 and CuNiSiCr demonstrated high miscibility, ensuring a sound metallurgical bond and a smooth transition. Although no cracks were observed, the presence of defects such as gas porosity and lack of fusion (LoF)—particularly within the CuNiSiCr alloy volume—highlights the need to further optimize printing parameters, not only for the individual alloy, but also within the transition zone.
- Across the transition region between Inconel-625 and CuNiSiCr, a gradual change in elemental concentrations was evident, with progressively decreasing levels of Ni, Cr, and Mo and a corresponding increase in Cu when moving from the Ni-base alloy to the Cu-base alloy. This transition occurs over a distance of approximately 2.8 mm, indicating significant elemental diffusion between the two materials. The macroscopically continuous interface between the two alloys assumes heterogeneous features at the microscopical scale, displaying grains of varying sizes (from coarse to extremely fine), depending on the local copper concentration. EDS maps gave evidence of the local flows of the distinct alloys within in the former molten pool, with copper preferentially occupying regions complementary to the primary elements of Inconel-625 (Ni, Cr, and Mo).
- The interaction between the almost mutual immiscible carbon steel substrate and CuNiSiCr resulted in the formation of a globular structure of the deposited Cu-base alloy close to the build plate, and in occasional vertical cracks attributed to the immiscibility of Cu in Fe and the infiltration of the liquid copper along the steel grain boundaries during solidification. Conversely, the interaction between carbon steel and Inconel-625 alloy produced a more continuous metallurgical bond, characterized by an interdiffusion zone where nickel played a role in promoting a fcc Fe-rich crystal structure.

CRediT authorship contribution statement

Federico Larini: Writing – original draft, Methodology, Investigation. **Riccardo Casati:** Writing – review & editing, Validation, Methodology, Conceptualization. **Silvia Marola:** Writing – review & editing, Validation, Investigation. **Maurizio Vedani:** Writing – review & editing, Validation, Methodology, Conceptualization.

Declaration of competing interest

The authors declare that they have no known competing financial interests or personal relationships that could have appeared to influence the work reported in this paper.

Acknowledgements

The authors would like to thank Rasheed Michael Ishola and Ludovica Rovatti for their invaluable contribution to the SEM analyses. This study was partially funded by MICS (Made in Italy – Circular and Sustainable) Extended Partnership and received funding from the European Union Next-GenerationEU (PIANO NAZIONALE DI RIPRESA E RESILIENZA (PNRR) – MISSIONE 4 COMPONENTE 2, INVESTIMENTO 1.3 – D.D. 1551.11-10-2022, PE00000004).

Data availability

Data will be made available on request.

References

[1] A. Nazir, O. Gokcekaya, K. Md Masum Billah, O. Ertugrul, J. Jiang, J. Sun, S. Hussain, Multi-material additive manufacturing: a systematic review of design, properties, applications, challenges, and 3D printing of materials and cellular metamaterials, Mater. Des. 226 (2023), https://doi.org/10.1016/j.matdes.2023.111661.
[2] B. Onuike, B. Heer, A. Bandyopadhyay, Additive manufacturing of Inconel 718—copper alloy bimetallic structure using laser engineered net shaping (LENSTM), Addit. Manuf. 21 (2018) 133–140, https://doi.org/10.1016/j.addma.2018.02.007.
[3] O.M. Al-Jamal, S. Hinduja, L. Li, Characteristics of the bond in Cu-H13 tool steel parts fabricated using SLM, CIRP Ann. Manuf. Technol. 57 (2008) 239–242, https://doi.org/10.1016/j.cirp.2008.03.010.
[4] D.C. Hofmann, S. Roberts, R. Otis, J. Kolodziejska, R.P. Dillon, J.O. Suh, A. A. Shapiro, Z.K. Liu, J.P. Borgonia, Developing gradient metal alloys through radial deposition additive manufacturing, Sci. Rep. 4 (2014), https://doi.org/10.1038/srep05357.
[5] D. Wang, L. Liu, G. Deng, C. Deng, Y. Bai, Y. Yang, W. Wu, J. Chen, Y. Liu, Y. Wang, X. Lin, C. Han, Recent progress on additive manufacturing of multi-material structures with laser powder bed fusion, Virtual Phys. Prototyp. 17 (2022) 329–365, https://doi.org/10.1080/17452759.2022.2028343.
[6] W. Meng, W. Zhang, W. Zhang, X. Yin, B. Cui, Fabrication of steel-Inconel functionally graded materials by laser melting deposition integrating with laser synchronous preheating, Opt. Laser Technol. 131 (2020), https://doi.org/10.1016/j.optlastec.2020.106451.
[7] Z.H. Liu, D.Q. Zhang, S.L. Sing, C.K. Chua, L.E. Loh, Interfacial characterization of SLM parts in multi-material processing: metallurgical diffusion between 316L stainless steel and C18400 copper alloy, Mater. Charact. 94 (2014) 116–125, https://doi.org/10.1016/j.matchar.2014.05.001.
[8] A. Marques, Ó. Carvalho, F.S. Silva, F. Bartolomeu, S. Pereira, P. Alexandrino, Inconel 718-Copper bimetallic joints fabricated by 3D multi-material laser powder bed fusion for aerospace components, n.d.
[9] M. Schneck, M. Horn, M. Schindler, C. Seidel, Capability of multi-material laser-based powder bed fusion—development and analysis of a prototype large bore engine component, Metals (Basel) 12 (2022), https://doi.org/10.3390/met12010044.
[10] M. Abdelhafiz, K.S. Al-Rubaie, A. Emadi, M.A. Elbestawi, Process–structure–property relationships of copper parts manufactured by laser powder bed fusion, Materials 14 (2021), https://doi.org/10.3390/ma14112945.
[11] S.D. Jadhav, L.R. Goossens, Y. Kinds, B. Van Hooreweder, K. Vanmeensel, Laser-based powder bed fusion additive manufacturing of pure copper, Addit. Manuf. 42 (2021), https://doi.org/10.1016/j.addma.2021.101990.
[12] M. Rabiee, H. Mirzadeh, A. Ataie, Processing of Cu-Fe and Cu-Fe-SiC nanocomposites by mechanical alloying, Adv. Powder Technol. 28 (2017) 1882–1887, https://doi.org/10.1016/j.apt.2017.04.023.
[13] S. Kou, Welding Solidifi cation and Liquation Cracking Issues in Welding, n.d.
[14] L. Liu, D. Wang, G. Deng, Y. Yang, J. Chen, J. Tang, Y. Wang, Y. Liu, X. Yang, Y. Zhang, Interfacial characteristics and formation mechanisms of copper–steel multimaterial structures fabricated via laser powder bed fusion using different building strategies, Chin. J. Mech. Eng.: Addit. Manuf. Front. 1 (2022) 100045, https://doi.org/10.1016/j.cjmeam.2022.100045.
[15] N.L. Mochel, Thermal Expansion of Metals, n.d. www.astm.org.
[16] J. Chen, Y. Yang, C. Song, M. Zhang, S. Wu, D. Wang, Interfacial microstructure and mechanical properties of 316L /CuSn10 multi-material bimetallic structure fabricated by selective laser melting, Mater. Sci. Eng. A 752 (2019) 75–85, https://doi.org/10.1016/j.msea.2019.02.097.
[17] S. Yadav, C.P. Paul, A.K. Rai, R. Singh, S.K. Dixit, Elucidating laser directed energy deposition based additive manufacturing of copper-stainless steel functionally graded material: processing and material behavior, J. Manuf. Process. 92 (2023) 107–123, https://doi.org/10.1016/j.jmapro.2023.02.041.
[18] X. Zhang, C. Sun, T. Pan, A. Flood, Y. Zhang, L. Li, F. Liou, Additive manufacturing of copper – H13 tool steel bi-metallic structures via Ni-based multi-interlayer, Addit. Manuf. 36 (2020), https://doi.org/10.1016/j.addma.2020.101474.
[19] M.A. Turchanin, P.G. Agraval, A.R. Abdulov, Phase equilibria and thermodynamics of binary copper systems with 3d-metals. VI. Copper-nickel System, 2007.
[20] A. Marques, Â. Cunha, M. Gasik, O. Carvalho, F.S. Silva, F. Bartolomeu, Inconel 718–copper parts fabricated by 3D multi-material laser powder bed fusion: a novel technological and designing approach for rocket engine, Int. J. Adv. Manuf. Technol. 122 (2022) 2113–2123, https://doi.org/10.1007/s00170-022-10011-x.
[21] L. Zhang, P. Dong, Y. Zeng, H. Yao, J. Chen, Additive manufacturing of Inconel 718/CuCrZr multi-metallic materials fabricated by laser powder bed fusion, Addit. Manuf. 92 (2024), https://doi.org/10.1016/j.addma.2024.104377.
[22] D. Yuan, X. Sun, J. Wang, Z. Zhang, D. Cheng, C. Wei, L. Li, Cracking behavior of IN718/Cu10Sn bimetallic structures fabricated by laser directed energy deposition with different deposition sequences, J. Alloys Compd. 1033 (2025), https://doi.org/10.1016/j.jallcom.2025.181222.
[23] G. Cacciamani, A. Dinsdale, M. Palumbo, A. Pasturel, The Fe-Ni system: thermodynamic modelling assisted by atomistic calculations, Intermetallics (Barking) 18 (2010) 1148–1162, https://doi.org/10.1016/j.intermet.2010.02.026.
[24] B. Aydogan, A. O'Neil, H. Sahasrabudhe, Microstructural and mechanical characterization of stainless steel 420 and Inconel 718 multi-material structures fabricated using laser directed energy deposition, J. Manuf. Process. 68 (2021) 1224–1235, https://doi.org/10.1016/j.jmapro.2021.06.031.
[25] Y. Li, Z. Liu, Z. Wei, P. Hu, J. Chen, L. Liu, G. Shu, J. Xie, Inhibition of interfacial cracks in 304L-Inconel718 bimetal fabricated via laser powder bed fusion, Addit. Manuf. 94 (2024), https://doi.org/10.1016/j.addma.2024.104463.
[26] N. Chen, H.A. Khan, Z. Wan, J. Lippert, H. Sun, S.L. Shang, Z.K. Liu, J. Li, Microstructural characteristics and crack formation in additively manufactured bimetal material of 316L stainless steel and Inconel 625, Addit. Manuf. 32 (2020), https://doi.org/10.1016/j.addma.2020.101037.
[27] H. Jia, H. Sun, H. Wang, Y. Wu, H. Wang, Scanning strategy in selective laser melting (SLM): a review, (n.d.). https://doi.org/10.1007/s00170-021-06810-3/Published.
[28] C.M. Cepeda-Jiménez, F. Potenza, E. Magalini, V. Luchin, A. Molinari, M.T. Pérez-Prado, Effect of energy density on the microstructure and texture evolution of Ti-6Al-4V manufactured by laser powder bed fusion, Mater Charact 163 (2020), https://doi.org/10.1016/j.matchar.2020.110238.
[29] A. Hess, R. Schuster, A. Heider, R. Weber, T. Graf, Continuous wave laser welding of copper with combined beams at wavelengths of 1030 nm and of 515 nm, Phys. Procedia, Elsevier B.v. (2011) 88–94, https://doi.org/10.1016/j.phpro.2011.03.012.
[30] H. Hyer, R. Newell, D. Matejczyk, S. Hsie, M. Anthony, L. Zhou, C. Kammerer, Y. Sohn, Microstructural development in as built and heat treated IN625 component additively manufactured by laser powder bed fusion, J. Phase Equilibria Diffus. 42 (2021) 14–27, https://doi.org/10.1007/s11669-020-00855-9.
[31] S. Gruber, L. Stepien, E. López, F. Brueckner, C. Leyens, Physical and geometrical properties of additively manufactured pure copper samples using a green laser source, Materials 14 (2021), https://doi.org/10.3390/ma14133642.
[32] T. Romano, A. Ratkus, S. Gruber, M. Pozzi, H. Kos, C. Garion, S. Rorison, E. López, T. Torims, M. Vedani, Pure copper membranes manufactured by green laser powder bed fusion with varying wall-thickness and building orientation: microstructure, properties, and vacuum tightness performance, Vacuum 233 (2025) 113995, https://doi.org/10.1016/j.vacuum.2024.113995.
[33] E. Fereiduni, A. Ghasemi, N. Sargent, M. Balbaa, L. Wang, M. Elbestawi, S.L. Sing, W. Xiong, Synergy of laser powder bed fusion (LPBF) and heat treatment for CuNi2SiCr alloy enhancement, Mater. Des. 255 (2025), https://doi.org/10.1016/j.matdes.2025.114189.
[34] Z. Tian, C. Zhang, D. Wang, W. Liu, X. Fang, D. Wellmann, Y. Zhao, Y. Tian, A review on laser powder bed fusion of inconel 625 nickel-based alloy, Appl. Sci. (Switzerland) 10 (2020), https://doi.org/10.3390/app10010081.
[35] K.B. Fillingim, R. Kannan, L. Heinrich, K. Saleeby, P. Nandwana, T. Feldhausen, Process parameter translation strategies for variable directed energy deposition spot size using 316L, copper, and Inconel 625, Heliyon 10 (2024), https://doi.org/10.1016/j.heliyon.2024.e37658.
[36] Y. Wen, B. Zhang, R.L. Narayan, P. Wang, X. Song, H. Zhao, U. Ramamurty, X. Qu, Laser powder bed fusion of compositionally graded CoCrMo-Inconel 718, Addit. Manuf. 40 (2021), https://doi.org/10.1016/j.addma.2021.101926.
[37] T. DebRoy, H.L. Wei, J.S. Zuback, T. Mukherjee, J.W. Elmer, J.O. Milewski, A. M. Beese, A. Wilson-Heid, A. De, W. Zhang, Additive manufacturing of metallic components – process, structure and properties, Prog. Mater Sci. 92 (2018) 112–224, https://doi.org/10.1016/j.pmatsci.2017.10.001.
[38] S. Nucci, Microstructural development of inconel 625 nickel-based superalloy as function of laser powder bed fusion, Parameters (2021). https://stars.library.ucf.edu/etd2020/538.
[39] B. Dubiel, J. Sieniawski, Precipitates in additively manufactured inconel 625 superalloy, Materials 12 (2019), https://doi.org/10.3390/ma12071144.
[40] J. Preis, D. Xu, B.K. Paul, P.A. Eschbach, S. Pasebani, Effect of liquid miscibility gap on defects in inconel 625–GRCop42 joints through analysis of gradient composition microstructure, J. Manuf. Mater. Process. 8 (2024), https://doi.org/10.3390/jmmp8010042.
[41] T. Romano, M. Abdelwahed, V. Bertolo, T. Cecotti, S. Skhosane, G. Mahadevan, V. Popovich, M. Hermans, M.A. Taha, S. Pityana, M. Vedani, Microstructural, mechanical, and thermal characterization of constitutive layers in copper-steel functionally graded material manufactured via laser directed energy deposition, Mater. Des. 256 (2025), https://doi.org/10.1016/j.matdes.2025.114329.
[42] H. Mohrbacher, A. Kern, Nickel alloying in carbon steel: fundamentals and applications, Alloys 2 (2023) 1–28, https://doi.org/10.3390/alloys2010001.
[43] Q. Tan, H. Chang, G. Liang, V. Luzin, Y. Yin, F. Wang, X. Cheng, M. Yan, Q. Zhu, C. Hutchinson, M.X. Zhang, High performance plain carbon steels obtained through 3D-printing, Nat. Commun. 15 (2024), https://doi.org/10.1038/s41467-024-54507-4.